

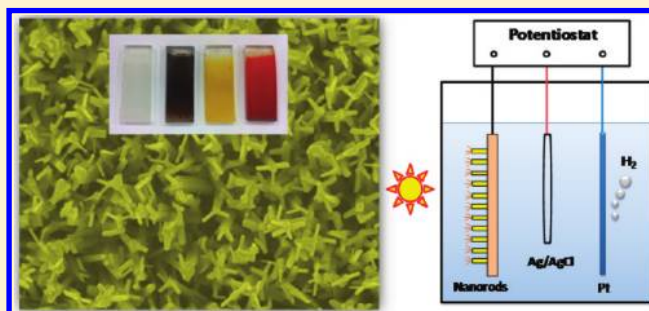
TiO₂/(CdS, CdSe, CdSeS) Nanorod Heterostructures and Photoelectrochemical Properties

Jingshan Luo,[†] Lin Ma,[†] Tingchao He,[†] Chin Fan Ng,[†] Shijie Wang,[‡] Handong Sun,[†] and Hong Jin Fan^{*†}

[†]Division of Physics and Applied Physics, School of Physical and Mathematical Sciences, Nanyang Technological University, Singapore 637371, Singapore

[‡]Institute of Materials Research and Engineering (IMRE), A*STAR (Agency for Science, Technology and Research), 3 Research Link, Singapore 117602

ABSTRACT: In this work, nanorods of CdS, CdSe, and CdSeS are deposited by chemical vapor deposition on TiO₂ nanorod arrays, and the photoelectrochemical (PEC) performance of the heterostructures is studied comprehensively. It is found that nanorods-shaped CdS are superior to nanoparticles as the photosensitizer. The difference in the photosensitizing effect to TiO₂ nanorods among CdS, CdSe, and CdSeS alloy nanorods is studied using optical and electrochemical techniques. The energy levels of these heterostructure photoelectrodes are constructed based on X-ray photoelectron spectroscopy (XPS) and diffused reflectance spectra measurements. The current–time profile with chopped light condition, in combination with time-resolved photoluminescence spectroscopy, reveals that the TiO₂/CdS electrode has the lowest carrier recombination rate, highest electron injection efficiency, and highest chemical stability. Nevertheless, in terms of the overall PEC performance (photocurrent level and stability), we propose the TiO₂/CdSSe electrode is most favorable.



1. INTRODUCTION

Solar light-driven water splitting by photoelectrochemical (PEC) cells offers an ideal route for H₂ generation due to sustainable solar energy and abundant water resources.^{1,2} Since the first report on the electrochemical photolysis of H₂O with TiO₂ as photoanode by Fujishima and Honda,³ research on water splitting has received increasing attention. TiO₂ has been one of the most attractive materials for this application because of its high photoactivity and low cost as well as excellent chemical stability.⁴ However, because of its large band gap (~3.2 eV), TiO₂ can only harvest the UV light which takes only 5% of sunlight, resulting in low energy conversion efficiency. Tremendous efforts have been paid to enhance its visible light harvesting ability. Typically, the methods can be summarized into two categories: One way is through band gap narrowing by element doping^{5–7} or introducing defect states within the forbidden band.⁸ Another strategy is sensitizing TiO₂ with narrow band-gap semiconductors such as CdS,^{9–12} CdSe,^{13,14} and PbS,^{15,16} which is widely employed in quantum-dot-sensitized solar cells (QDSSCs). Among various chalcogenides compounds, CdS and CdSe are the most commonly studied sensitizers due to their small band gap of 2.4 and 1.7 eV, respectively, and the synergistic effect of cosensitization.¹⁷

Various methods have been developed for sensitization, mainly in two approaches, postsynthesis assembly, and direct growth. In the first method, presynthesized quantum dots (QDs) are bound to TiO₂ through organic molecule linkers.¹⁸ The latter method (direct growth) includes chemical bath

deposition,^{12,19} successive ionic layer adsorption and reaction (SILAR),¹⁴ electrochemical deposition,⁹ and chemical vapor deposition (CVD).^{11,20} The solution-based deposition is most commonly used for sensitizing TiO₂-based PEC anodes. However, loading of the sensitizer by the solution method is generally low, and the charge transfer from sensitizer to TiO₂ could be negatively affected due to the chemical species at the interface of the sensitizer and TiO₂. Direct growth of the sensitizer on TiO₂ by CVD provides a compact physical contact to favor charge transfer, a facial way to increase the loading of the sensitizer, and high crystalline structure.

Albeit there are a large number of publications on CdS- and CdSe-sensitized TiO₂ PEC photoelectrodes,^{12,17,21} little attention²² has been paid to the effect of the morphology of the sensitizer on the PEC performance and comparing the stability and charge transfer dynamics of different Cd-based semiconductor sensitizers. In contrast to nanoparticles, nanorods possess several advantages, including higher surface areas, easier electron–hole charge separation and thus efficient electron injections, and larger optical absorption cross section;^{17,23,24} all are beneficial to the PEC performance. Furthermore, cadmium chalcogenides differ in themselves in terms of the band gap, energy level, chemical stability, and

Received: April 3, 2012

Revised: May 12, 2012

Published: May 17, 2012

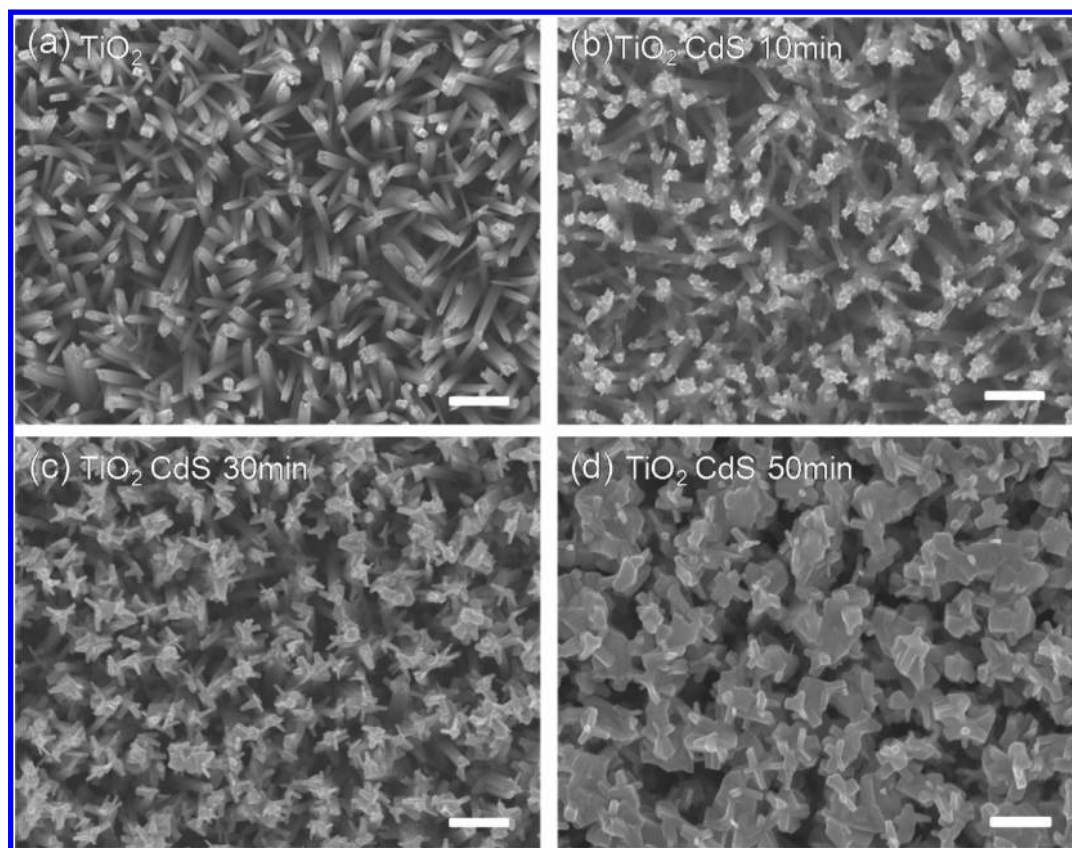


Figure 1. SEM images of the nanostructures. (a) TiO_2 nanorod array grown on FTO. (b) After CVD of CdS for 10 min. TiO_2 nanorods are covered by CdS nanoparticles on their tops due to preferential nucleation at the rough tips of the TiO_2 nanorods. (c) After CVD of CdS for 30 min. CdS nanoparticles grow into short nanorods. (d) After CVD of CdS for 50 min with coalescence of the short rods. Scale bars are 300 nm.

therefore photosensitizing effect in PEC electrode. A comprehensive investigation of these differences is desirable.

In this paper, we first deal with the shape effect of the CdS on quasi-aligned TiO_2 nanorod arrays by comparing three different nanostructures. It is found that nanorods have a superior sensitizing effect on nanoparticles. We then fabricate CdSe and CdSeS alloy nanorods heterostructured with TiO_2 nanorods array electrodes. Through systematic PEC and optical characterization, insights to the advantages and drawbacks of these cadmium chalcogenides nanorods in terms of chemical stability and interface electron injection efficiency are obtained. Our results provide useful information on structure design and rational selection of suitable photosensitizers on TiO_2 nanorod array-based electrodes toward efficient solar fuel cells.

2. EXPERIMENTAL SECTION

Preparation of TiO_2 Nanorod Array. TiO_2 nanorod arrays on transparent conductive fluorine-doped tin oxide (FTO) were synthesized by a hydrothermal growth method according to the literature.²⁵ In a typical process, the FTO substrates were first cleaned with acetone, ethanol, and deionized water for 5 min, respectively, and then dried by N_2 stream. The precursor was prepared by adding 0.45 mL of titanium butoxide to a well-mixed solution containing 15 mL of HCl and 15 mL of H_2O , and then the whole mixture was stirred for another 10 min until the solution became clear. Afterward, the precursor was poured into a Teflon-liner stainless steel autoclave with the FTO substrates placed at an angle against the wall with the conductive side facing down. Hydrothermal growth was conducted at 150 °C for 12 h in an

electric oven. Afterward, the FTO substrates were rinsed with deionized water and dried in ambient air.

CVD Deposition of CdS, CdSe, and CdSeS. Deposition of CdS, CdSe, and CdSeS on TiO_2 nanorod arrays was conducted by CVD based on a vapor–solid process without using metal catalyst.²⁶ The powder of CdS and CdSe precursor was put into a quartz boat loaded into the center of a 1 in. diameter quartz tube placed in a horizontal tube furnace. For the CdSeS alloy sample, considering the lower melting point of CdSe than CdS, CdSe powder was positioned at the upstream inside the quartz-tube furnace to make sure that the CdSe can vaporize with the CdS at a similar speed. FTO substrates grown with the TiO_2 nanorod arrays were put a few centimeters away from the source. Hydrogen diluted with argon (volume ratio 2%) served as the carrier gas with a flow rate of 10 sccm. The pressure was kept at 10 mbar. The precursor was heated to 700 °C at a rate of 25 °C/min and kept at the peak temperature for 10, 30, and 50 min for different samples before cooling down naturally to room temperature.

Structural and Optical Characterization. The morphology of the samples was characterized using a JEOL JSM-6700F field emission scanning electron microscope (SEM). X-ray diffraction (XRD) patterns were recorded by a Bruker D8 Advanced diffractometer with $\text{Cu K}\alpha$ as the radiation source. UV–vis absorption spectra were recorded by a Cary 100 UV–vis spectrophotometer. Diffused reflectance spectra were recorded by a Zolix Solar Cell QE/IPCE measurement system equipped with an integrated sphere and a Si diode. For steady state photoluminescence (PL) measurement, the 325 nm line from a He–Cd laser was used as the excitation source. Time-

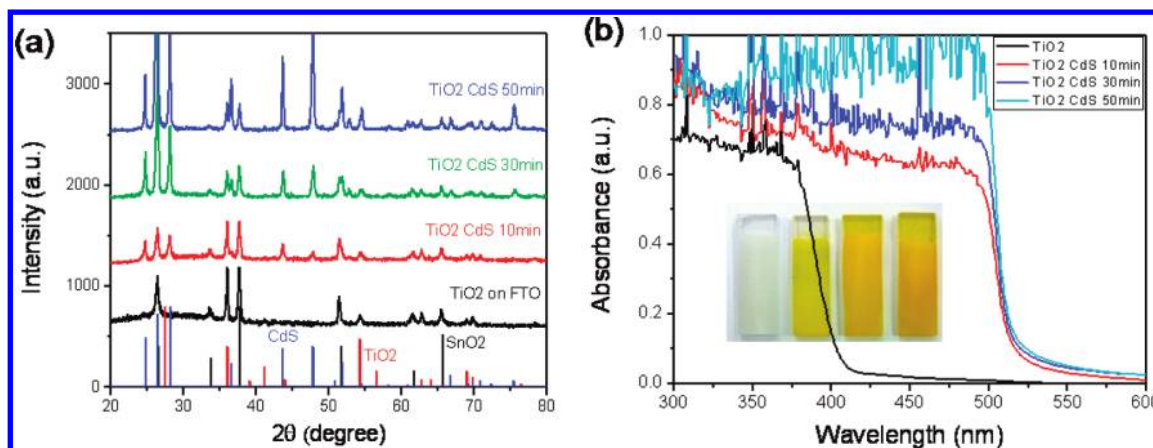


Figure 2. (a) XRD patterns of the samples. Vertical lines are from calculation. Green, wurtzite CdS; black, rutile SnO₂; red, rutile TiO₂. (b) UV-vis absorption spectra of the pristine TiO₂ nanorod array and the CdS-sensitized TiO₂ nanorod arrays. (Inset) Photograph of the corresponding samples on FTO/glass.

resolved photoluminescence spectra (TRPL) measurements were carried out using the time-correlated single-photon counting (TCSPC) technique with a resolution of 10 ps (Pico-Quant PicoHarp 300). The second harmonic of the titanium sapphire laser (Chameleon, Coherent Inc.) at 450 nm (100 fs, 80 MHz) was used as the excitation source. The signal was measured at the wavelength of the correlated steady state PL peak. XPS measurements were performed in a VG ESCALAB 220i-XL system using a monochromatic Al K α_1 source (1486.6 eV). All XPS spectra were obtained in the constant pass energy (CPA) mode. The pass energy of the analyzer was set to 10 eV in order to have high measurement accuracy. The binding energy scale was calibrated with pure Au, Ag, and Cu by setting Au 4f_{7/2}, Ag 3d_{5/2}, and Cu 2p_{3/2} at binding energies of 83.98, 368.26, and 932.67 eV, respectively.

Photoelectrochemical Measurements. Photoelectrochemical measurements were carried out in a three-electrode configuration with the as-prepared sample as the working electrode, Pt foil as the counter electrode, and saturated Ag/AgCl as the reference electrode. A mixture of 0.35 M Na₂SO₃ and 0.25 M Na₂S (pH = 12.4 tested by the Sartorius PB-11 pH meter) aqueous solution was used as the electrolyte and sacrificial reagent to maintain the stability of CdS and CdSe.¹⁷ Before experiment, the solution was purged by argon to remove the dissolved oxygen. A 150 W Xe lamp (Sciencetech SS 150 Solar Simulator) equipped with an AM 1.5G filter was used as the light source. The intensity of the incident light was calibrated with a standard Si solar cell and controlled at 100 mW/cm². The current density versus potential (*J*-*V*) curve of the working electrode was carried out by the linear sweep voltammograms with a potentiostat (CHI760D CH Instruments) at a scan rate of 10 mV/s. The photoresponses of the different samples were carried out by potentiostatic (current vs time, *I*-*t*) measurements under intermittent illumination at a bias of 0 V versus Ag/AgCl electrode. The incident photon to current efficiency (IPCE) was measured using a Zolix Solar Cell QE/IPCE measurement system with a standard silicon solar cell as the reference in the three-electrode configuration at 0 V versus Ag/AgCl electrode.

3. RESULTS AND DISCUSSION

3.1. Optimizing the Structure of CdS on TiO₂ Nanorod Array. TiO₂ nanorod arrays on FTO were fabricated by

hydrothermal growth, during which a low precursor concentration was used in order to obtain a relatively low density nanorod array (higher precursor concentration would result in severe bundling of the nanorods). The nanorods are quasi-aligned and have diameters of about 100 nm and lengths of about 1.5 μ m as revealed by the SEM images in Figure 1a, and the tips of the nanorods are rougher compared to their side faces due to axial growth. For subsequent deposition of CdS, the source temperature was maintained at 700 °C and the FTO substrates with TiO₂ nanorod arrays were put at the outlet of the furnace with a temperature around 500 °C. Figure 1b–d shows the morphology of CdS-modified TiO₂ nanorod arrays in different deposition times. With a deposition time of 10 min, small CdS nanoparticles are formed on the top part of the TiO₂ nanorods due to preferential nucleation. Nanoparticles grow into the short nanorod structure as the deposition time increases to 30 min. Further increasing the deposition time to 50 min causes formation of CdS to be large irregular-shaped aggregates (for convenience, we call them nanostumps) covering the entire TiO₂ tips.

It is known that vapor–solid (VS) is a typical nanorod growth mechanism occurring at high-temperature deposition for various materials including metal oxides.^{27–30} The resulting morphology is sensitively dependent on growth parameters such as the vapor pressure (a higher partial pressure is generally required for a high supersaturation), temperature (affect dynamics), and substrate feature (e.g., a defect-rich surface is more favorable for nucleation and deposition than flat ones). In our case, initial nucleation of CdS takes place preferentially at the tips of the TiO₂ nanorods as assisted by their high roughness. These nanoparticles serve as the seed for the next-stage anisotropic growth of short rods. VS growth of rod-shaped nanostructure is typical for wurtzite crystals including ZnO.³¹ As the deposition time increases, due to the increased overall surface roughness and reduced available space, VS deposition of CdS occurs preferentially at the irregular sites which are the gaps between the short CdS nanorods, causing a merged growth into a less anisotropic morphology similar to a stump.

XRD was conducted to characterize the phase and crystallinity of both pristine TiO₂ nanorod arrays and CdS-decorated samples. The patterns are illustrated in Figure 2a. Hydrothermal-grown TiO₂ nanorod arrays have a rutile

structure (JCPDS card no. 21-1276), and the deposited CdS nanoparticle, nanorod, and nanostump structures show an identical hexagonal wurtzite structure (JCPDS card no. 41-1049), which is in accordance with the previous report.^{9,32} The intensity of the diffraction peaks of CdS increases with increasing deposition time, which indicates the loading of CdS could be tuned by varying the deposition time. UV–vis absorption spectra were recorded to test the light-harvesting capability of both the pristine and the CdS-decorated TiO₂ nanorod arrays. Due to the wide band gap of TiO₂, the pristine nanorod array could only absorb up to 410 nm as shown in Figure 2b. After sensitization with CdS, the absorption range broadens to 520 nm. In addition, UV–vis absorption spectra also show that as the CdS deposition time increases the light absorption ability also increases.

The type II band alignment between CdS and TiO₂ is favorable for transfer of photogenerated electrons from CdS to TiO₂.³³ This is one of the reasons that makes the CdS and other cadmium chalcogenides suitable photosensitizers for TiO₂ as PEC photoanodes. To characterize the ability of the samples for PEC cells, linear sweep voltammograms were recorded both in the dark and with simulated solar light illumination condition to show the *J*–*V* curves. As shown in Figure 3, all electrodes show negligible current under dark

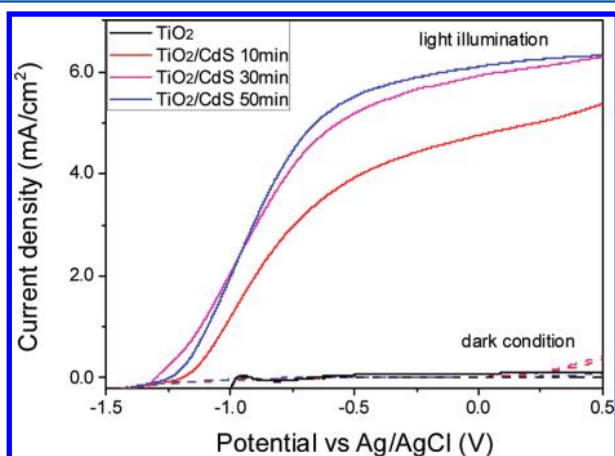


Figure 3. *J*–*V* curves of the pristine TiO₂ nanorod array and CdS sensitized TiO₂ samples under dark condition and simulated solar light illumination.

condition. With light illumination, pristine TiO₂ nanorod array has a current density of 0.13 mA/cm² at 0 V versus Ag/AgCl. In comparison, the CdS nanorod-sensitized TiO₂ shows a current density of 5.8 mA/cm², which is nearly 45 times higher than the pristine TiO₂ electrode. The great enhancement of the photocurrent after CdS sensitization shows the advantage of the CVD compared to the solution process which has a photocurrent of 5.1 mA/cm².¹⁷ For pristine TiO₂, the onset potential is only around –0.85 V. After CdS sensitization, this value shifted to around –1.25 V, which indicates a shift in Fermi level to more negative potential as a result of the coupling between TiO₂ and CdS in the composite system. Among the three types of CdS morphologies, CdS loading increases from nanoparticle, to nanorod, and to nanostump. Their photocurrent densities follow the same trend, except that the nanostump-sensitized sample has only a slight increase in the current density compared to the nanorod-sensitized one. A higher photocurrent would correspond to a higher efficiency of

the PEC device for solar hydrogen generation, as the current is related to the electrons needed to reduce the H⁺ ions into H₂ at the Pt cathode.

For a high PEC performance, loading of the sensitizer needs to balance with the charge recombination loss. In general, a higher loading of the photosensitizer will increase the density of carriers leading to a higher photocurrent density.³⁴ On the other hand, as previously reported, an increased sensitizer loading is also accompanied with a higher internal recombination rate within the sensitizer³⁵ and a thicker coating of the sensitizer would also reduce the surface area of the photoanode.³⁶ Both of these two factors would lower the overall efficiency. In our experiment, though the nanostump structure has an evidently higher CdS loading than the nanorods, the increase of the photocurrent level is only marginal. This may be due to the negative contribution of the higher internal recombination rate as well as a reduction of the surface area as mentioned above. Therefore, taking the cost of CdS and the thermal budget into consideration, a further increase of CdS loading by prolonged deposition was not attempted in our study; the nanorod structure will be adopted for other cadmium chalcogenide sensitizers in the rest of this study.

3.2. Comparison between CdS, CdSe, and CdSeS Nanorod Sensitizers. In this section we deal with other Cd-based narrow band-gap semiconductors as the photosensitizer of TiO₂. CdSe is commonly used as a cosensitizer together with CdS because of its much narrower band gap (1.73 eV), albeit a lower conduction band position than CdS.³⁷ Furthermore, CdSeS alloy semiconductor has a special advantage as a sensitizer in that its band gap is variable by tuning the composition.²⁰ Following the preceding part, nanorod structures of CdSe and CdSeS alloy were deposited onto TiO₂ nanorod array under the same condition as that for CdS. SEM images in Figure 4a–c show that the morphology of the formed nanorod heterostructures is nearly the same. According to the X-ray diffraction data in Figure 4d, the as-deposited CdSe nanorod has the same hexagonal wurtzite structure as CdS. The diffraction peaks of CdSeS lie between those of CdS and CdSe, which indicates that the CdS and CdSe components are thermodynamically miscible to form the alloy. Diffused reflectance spectra were recorded to reveal the light absorption capability of all photoelectrodes (see Figure 5). Clearly, the absorption range is further increased to 720 nm by coating TiO₂ with CdSe as sensitizer. For the CdSeS alloy sample, absorption cuts off at ~600 nm in the current sample, between those of CdS and CdSe. The exact composition is unknown but it is not of major concern for its application as photoelectrode. The band gaps of the different electrodes can be estimated by linear extrapolation of the absorption peaks to the baselines, which are 3.03, 2.39, 1.73, and 2.07 eV for the TiO₂, TiO₂/CdS, TiO₂/CdSe, and TiO₂/CdSeS electrodes, respectively.

The PEC properties of the above three photoanodes are compared. The linear sweep voltammograms (*J*–*V* curve) are illustrated in Figure 6a. The CdSe-sensitized electrode shows the highest photocurrent, around 9 mA/cm² at 0 bias versus Ag/AgCl. However, there is a peak at the saturated photocurrent plateau which could be due to photocorrosion and will be discussed later. The CdSeS alloy-sensitized electrode with a photocurrent of 8 mA/cm² takes second place compared to 6 mA/cm² of the CdS sample. One can also see that the CdS- and CdSeS-sensitized samples have the same onset potential of –1.3 V vs Ag/AgCl. In contrast, the onset potential of the CdSe-sensitized electrode is around –1.1 V, which can be

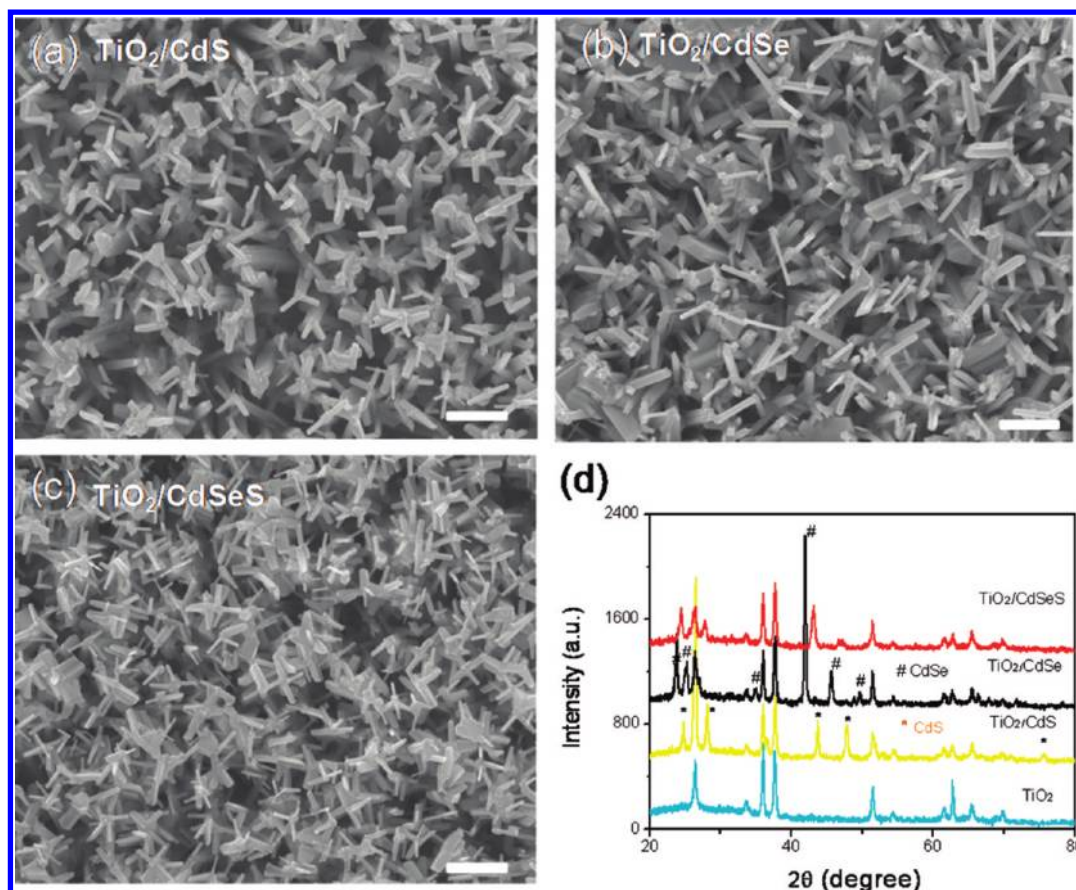


Figure 4. SEM images of the CVD CdS, CdSe, and CdSeS for 30 min on top of the TiO_2 nanorod array and their corresponding XRD patterns: (a) TiO_2/CdS , (b) TiO_2/CdSe , (c) $\text{TiO}_2/\text{CdSeS}$, and (d) XRD patterns of the as-prepared samples.

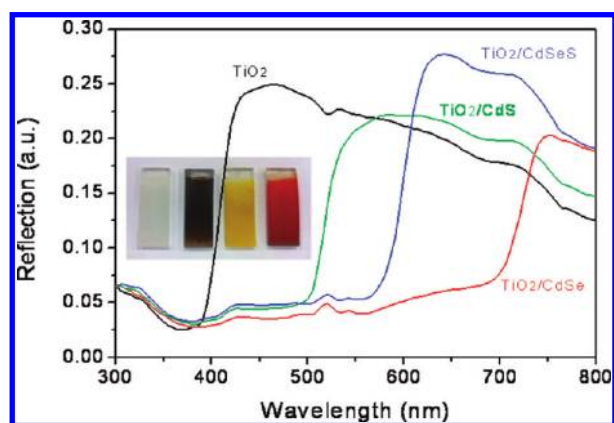


Figure 5. Diffuse reflectance spectra of the pristine TiO_2 nanorod array and CdS, CdSe, and CdSeS nanorod-sensitized TiO_2 nanorod arrays. (Inset) Photographs of the as-prepared samples.

ascribed to the lower conduction band edge of CdSe compared to CdS and CdSeS (see also Figure 7). To characterize the photoactivity of the electrodes at various wavelengths, the incident photon to current conversion efficiency (IPCE) test was carried out. The results in Figure 6b show that the response range of IPCE for each electrode is in accordance with the corresponding diffused reflectance spectrum in Figure 5. The IPCE of the CdS- and CdSeS-sensitized electrodes are round 55% across the absorption ranges, which are higher than the CdSe sample, indicating that electron–hole pairs are separated more efficiently in the CdS- and CdSeS-sensitized electrodes.

However, the CdSe sample exhibits a wider response range than the former two. This may be the reason why that CdSe/ TiO_2 electrode has the highest photocurrent.

In order to show the photoresponse and stability of the electrodes, photocurrent versus time ($J-t$) curves were recorded in chopped light illumination. From the results in Figure 6c, the currents of all electrodes are nearly zero in the dark condition and have a transient increase after illumination, which reveals their good photoresponses. However, for the TiO_2/CdSe and $\text{TiO}_2/\text{CdSeS}$ electrodes, the photocurrents show a sharp decrease especially at the first few cycles. This phenomenon is due to carrier recombination according to Kamat;³⁸ the TiO_2/CdSe electrode has the highest magnitude of decrease as a result of the highest recombination rate in CdSe. With prolonged measurement, the CdS- and CdSeS-sensitized electrodes maintain stable photocurrents. However, the current of the CdSe-sensitized electrode is the least stable and drops drastically in a few minutes. The results of the stability of the electrodes are in accordance with the general trend that the narrower the band gap of the material the less stable the material is.³⁹

In addition to the absorption range which controls the light-harvesting capability, the conduction band level is another important parameter that determines the onset potential and electron injection efficiency. XPS is a powerful technique to characterize the valence band maximum (VBM) of a semiconductor. The valence band spectra of the different electrodes were studied by XPS, and the results are illustrated in Figure 7a. The VBM of each electrode is derived by the linear

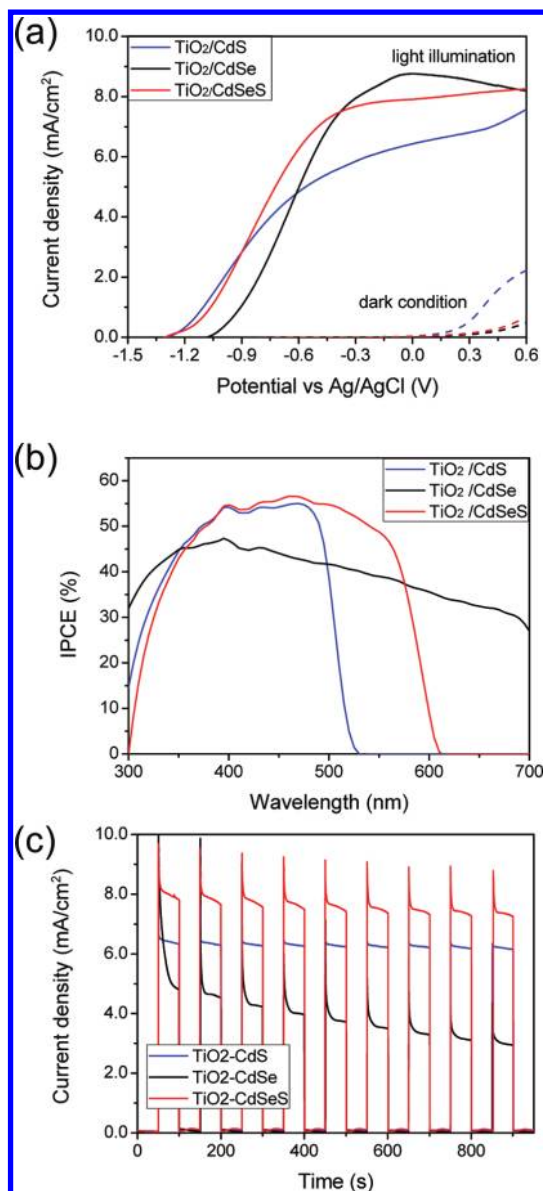


Figure 6. Photoelectrochemical properties of the TiO_2/CdS , TiO_2/CdSe , and $\text{TiO}_2/\text{CdSeS}$ nanorod electrodes. (a) J - V curves. (b) IPCE spectra at a potential of 0 V versus Ag/AgCl. (c) Time-dependent photocurrents and cycle stability test measured with the potential bias of 0 V versus Ag/AgCl under chopped light irradiation.

extrapolation method to be 2.67, 1.70, 1.25, and 1.42 eV below the Fermi level for the TiO_2 , TiO_2/CdS , TiO_2/CdSe , and $\text{TiO}_2/\text{CdSeS}$ electrodes, respectively. On the basis of the results of the band gap and the VBM, the positions of the conduction band minimum (CBM) could be determined. Figure 7b shows the band diagrams of each heterostructure electrode from the above-obtained band gap and CBM values. As seen, the conduction band level of the $\text{TiO}_2/\text{CdSeS}$ is very close to that of the TiO_2/CdS . The CBM of the TiO_2/CdSe is around 0.2 eV lower, which is in agreement with the onset potential difference determined from the J - V curves (Figure 6). Recently, Kamat reported that CdSe would undergo photo-transformation when in contact with the aqueous sulfide solution (which is the case in our system),⁴⁰ forming a thin layer of CdSeS alloy on top of the electrode. As the valence band of CdSeS alloy is lower than CdSe, the layer would inhibit hole transfer and thus result in lower photocurrent after a few minutes (see Figure 6c).

The charge separation and transfer mechanism is the internal process that determines the photocurrent and open-circuit potential of the electrode. This process can be revealed by measuring the electron injection efficiency by steady state and time-resolved photoluminescence (TRPL) spectroscopy.^{37,41} Figure 8a shows the steady state PL spectra recorded at the same excitation intensity using the 325 nm line from a He-Cd laser as the excitation source. Pristine TiO_2 has a nearly undetectable PL signal across the measurement range compared to the intense emissions from the cadmium chalcogenides, which is not surprising since TiO_2 is an indirect wide band-gap semiconductor. From the intensities of the band-gap emissions, the order of the recombination rate can be determined to be $\text{TiO}_2/\text{CdSe} > \text{TiO}_2/\text{CdSeS} > \text{TiO}_2/\text{CdS}$. TRPL measurements were carried out at room temperature to characterize the electron injection efficiency in detail. The signal was measured at the wavelength of the correlated steady state PL peak, which is 510, 580, and 700 nm for the CdS-, CdSeS alloy-, and CdSe-sensitized TiO_2 nanorods. Figure 8b shows the corresponding TRPL curves of the different electrodes and clearly reveals that CdS-sensitized electrode has the shortest PL lifetime among these three, which means that the carrier transfer from CdS toward TiO_2 is most efficient. The three exponential decay-fitting analyses of the obtained curves reveal that the averaged photoluminescence lifetime of these samples are 19 ps for TiO_2/CdS , 220 ps for TiO_2/CdSe , and 58 ps for $\text{TiO}_2/\text{CdSeS}$, which are much faster than the

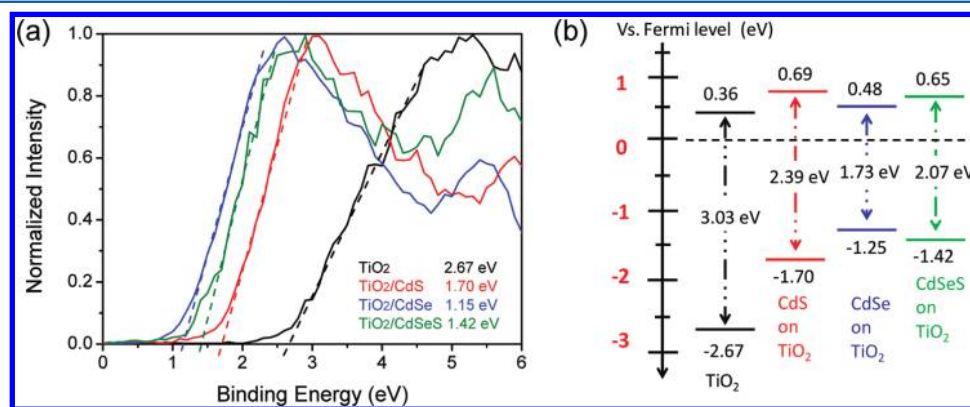


Figure 7. (a) Normalized XPS valence band spectra of the TiO_2 , TiO_2/CdS , TiO_2/CdSe , and $\text{TiO}_2/\text{CdSeS}$ electrodes. The valence band positions with reference to their Fermi levels are labelled. (b) Band diagram versus Fermi level.

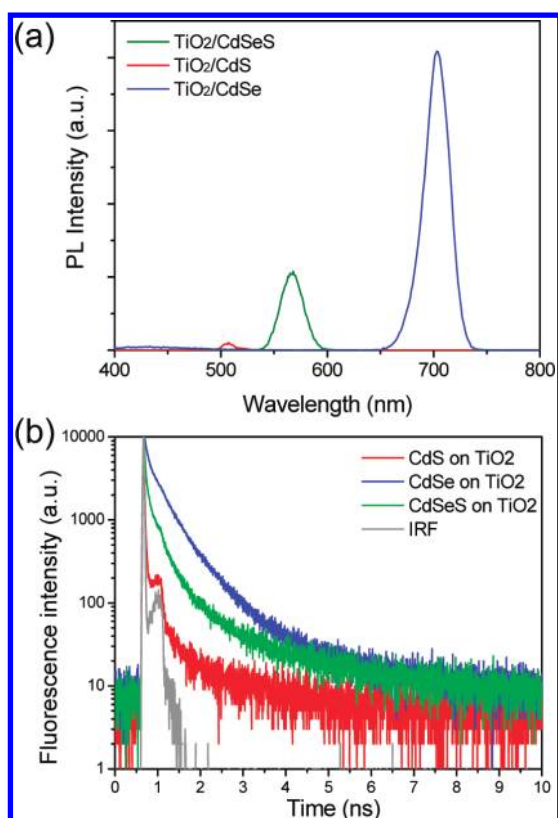


Figure 8. (a) Steady state PL spectra of the TiO_2/CdS , TiO_2/CdSe , and $\text{TiO}_2/\text{CdSeS}$ electrodes at an excitation wavelength of 325 nm with a He–Cd laser. (b) TRPL spectra of the TiO_2/CdS , TiO_2/CdSe , and $\text{TiO}_2/\text{CdSeS}$ electrodes recorded at their corresponding steady state PL peak wavelengths.

reported sensitization by the SILAR method,^{37,41} implying that the heterointerface by CVD is more efficient for electron injection than the one by the solution-based method. The lowest electron injection efficiency for the TiO_2/CdSe electrode indicated the potential chance for phototransformation discussed above. This result is in accordance with the amperometric J – t data (Figure 6c) and the conduction band edge position of the different electrodes (Figure 7a).

With an optimized CVD condition, it is possible to achieve a more homogeneous coating of the TiO_2 nanorods with cadmium chalcogenides and form core–shell heterogeneous nanowires. As a result of the increased interface areas and interface uniformity, it is envisaged that the IPCE values will be further improved, leading to an enhanced PEC performance. This work is currently underway.

4. CONCLUSION

Nanorods of CdS, CdSe, and CdSeS are deposited onto TiO_2 nanorod arrays as the photoelectrochemical electrode, which are studied thoroughly using optical and electrochemical techniques. A clear picture of the physical processes including charge injection efficiency, band alignment, stability, as well as effect of sensitizer morphology is presented. First, when the CdS is changed from particle, to rod, to stump-shaped morphology, the latter two TiO_2 anodes have evidently higher photocurrent densities compared to the nanoparticle sample, which could be a result of competition between light absorption, recombination loss, and surface areas. Among the three types of cadmium chalcogenides nanorod sensitizers, it is

found that (i) while the TiO_2/CdSe electrode has the highest initial photocurrent due to the smallest band gap, the current degrades quickly to the lowest one. Maintenance of its high photocurrent may need surface passivation. (ii) The TiO_2/CdS electrode has the lowest photocurrent but the highest electron injection efficiency, as revealed by the TRPL measurement. (iii) In terms of the photocurrent level and stability, the $\text{TiO}_2/\text{CdSeS}$ heterostructure would be a favorable choice. Further improvement could be realized by the conformal coating of the nanorod-shaped sensitizer around the entire TiO_2 nanorod surface using, for example, atomic layer deposition.

AUTHOR INFORMATION

Corresponding Author

*E-mail: fanhj@ntu.edu.sg.

Notes

The authors declare no competing financial interest.

REFERENCES

- (1) Das, K.; De, S. K. *J. Phys. Chem. C* **2009**, *113*, 3494.
- (2) Lewis, N. S.; Nocera, D. G. *Proc. Natl. Acad. Sci* **2006**, *103*, 15729.
- (3) Fujishima, A.; Honda, K. *Nature* **1972**, *238*, 37.
- (4) Chen, X.; Mao, S. S. *Chem. Rev.* **2007**, *107*, 2891.
- (5) Khan, S. U. M. *Science* **2002**, *297*, 2243.
- (6) Asahi, R. *Science* **2001**, *293*, 269.
- (7) Yu, J. C.; Yu, J. G.; Ho, W. K.; Jiang, Z. T.; Zhang, L. Z. *Chem. Mater.* **2002**, *14*, 3808.
- (8) Chen, X.; Liu, L.; Yu, P. Y.; Mao, S. S. *Science* **2011**, *331*, 746.
- (9) Misra, M.; Banerjee, S.; Mohapatra, S. K.; Das, P. P. *Chem. Mater.* **2008**, *20*, 6784.
- (10) Li, J. H.; Wang, H.; Bai, Y. S.; Zhang, H.; Zhang, Z. H.; Guo, L. *J. Phys. Chem. C* **2010**, *114*, 16451.
- (11) Lee, J.-C.; Kim, T. G.; Lee, W.; Han, S.-H.; Sung, Y.-M. *Cryst. Growth Des.* **2009**, *9*, 4519.
- (12) Niitsoo, O.; Sarkar, S. K.; Pejou, C.; Rühle, S.; Cahen, D.; Hodes, G. *J. Photochem. Photobiol. A: Chem.* **2006**, *181*, 306.
- (13) Kamat, P. V.; Kongkanand, A.; Tvrdy, K.; Takechi, K.; Kuno, M. *J. Am. Chem. Soc.* **2008**, *130*, 4007.
- (14) Lee, H.; Wang, M. K.; Chen, P.; Gamelin, D. R.; Zakeeruddin, S. M.; Grätzel, M.; Nazeeruddin, M. K. *Nano Lett.* **2009**, *9*, 4221.
- (15) Kramer, I. J.; Levina, L.; Debnath, R.; Zhitomirsky, D.; Sargent, E. H. *Nano Lett.* **2011**, *11*, 3701.
- (16) Lee, H.; Leventis, H. C.; Moon, S.-J.; Chen, P.; Ito, S.; Haque, S. A.; Torres, T.; Nüesch, F.; Geiger, T.; Zakeeruddin, S. M.; Grätzel, M.; Nazeeruddin, M. K. *Adv. Funct. Mater.* **2009**, *19*, 2735.
- (17) Lee, Y.-L.; Chi, C.-F.; Liao, S.-Y. *Chem. Mater.* **2010**, *22*, 922.
- (18) Guijarro, N.; Lana-Villarreal, T.; Mora-Sero, I.; Bisquert, J.; Gomez, R. *J. Phys. Chem. C* **2009**, *113*, 4208.
- (19) Chang, C.-H.; Lee, Y.-L. *Appl. Phys. Lett.* **2007**, *91*, 053503.
- (20) Park, J.; Myung, Y.; Jang, D. M.; Sung, T. K.; Sohn, Y. J.; Jung, G. B.; Cho, Y. J.; Kim, H. S. *ACS Nano* **2010**, *4*, 3789.
- (21) Cheng, S. L.; Fu, W. Y.; Hai, B. Y.; Zhang, L. N.; Ma, J. W.; Zhao, H.; Sun, M. L.; Yang, L. H. *J. Phys. Chem. C* **2012**, *116*, 2615.
- (22) Salant, A.; Shalom, M.; Tachan, Z.; Buchbut, S.; Zaban, A.; Banin, U. *Nano Lett.* **2012**, *12*, 2095.
- (23) Kuno, M.; Giblin, J. *J. Phys. Chem. Lett.* **2010**, *1*, 3340.
- (24) Garnett, E. C.; Brongersma, M. L.; Cui, Y.; McGehee, M. D. *Annu. Rev. Mater. Res.* **2011**, *41*, 269.
- (25) Aydil, E. S.; Liu, B. J. *Am. Chem. Soc.* **2009**, *131*, 3985.
- (26) Zhang, J.; Jiang, F. H.; Zhang, L. D. *J. Phys. Chem. B* **2004**, *108*, 7002.
- (27) Wu, X. C.; Tao, Y. R. *J. Cryst. Growth* **2002**, *242*, 309.
- (28) Shen, G. Z.; Lee, C. J. *Cryst. Growth Des.* **2005**, *5*, 1085.
- (29) Yamai, I.; Saito, H. *J. Cryst. Growth* **1978**, *45*, 511.
- (30) Umar, A.; Kim, S.; Lee, Y.; Nahm, K.; Hahn, Y. J. *Cryst. Growth* **2005**, *282*, 131.

- (31) Fan, H. J.; Scholz, R.; Kolb, F. M.; Zacharias, M.; Gosele, U.; Heyroth, F.; Eisenschmidt, C.; Hempel, T.; Christen, J. *Appl. Phys. A: Mater. Sci. Process.* **2004**, *79*, 1895.
- (32) Matsumura, M.; Furukawa, S.; Saho, Y.; Tsubomura, H. *J. Phys. Chem.* **1985**, *89*, 1327.
- (33) Shi, J.; Chen, J.; Feng, Z.; Chen, T.; Lian, Y.; Wang, X.; Li, C. *J. Phys. Chem. C* **2006**, *111*, 693.
- (34) Mora-Sero, I.; Bisquert, J. *J. Phys. Chem. Lett.* **2010**, *1*, 3046.
- (35) Mora-Sero, I.; Gimenez, S.; Fabregat-Santiago, F.; Gomez, R.; Shen, Q.; Toyoda, T.; Bisquert, J. *Acc. Chem. Res.* **2009**, *42*, 1848.
- (36) Mora-Sero, I.; Gonzalez-Pedro, V.; Xu, X. Q.; Bisquert, J. *ACS Nano* **2010**, *4*, 5783.
- (37) Chi, C. F.; Cho, H. W.; Teng, H. S.; Chuang, C. Y.; Chang, Y. M.; Hsu, Y. J.; Lee, Y. L. *Appl. Phys. Lett.* **2011**, *98*, 012101.
- (38) Robel, I.; Subramanian, V.; Kuno, M.; Kamat, P. V. *J. Am. Chem. Soc.* **2006**, *128*, 2385.
- (39) van de Krol, R.; Liang, Y. Q.; Schoonman, J. *J. Mater. Chem.* **2008**, *18*, 2311.
- (40) Chakrapani, V.; Baker, D.; Kamat, P. V. *J. Am. Chem. Soc.* **2011**, *133*, 9607.
- (41) Lin, K. H.; Chuang, C. Y.; Lee, Y. Y.; Li, F. C.; Chang, Y. M.; Liu, I. P.; Chou, S. C.; Lee, Y. L. *J. Phys. Chem. C* **2012**, *116*, 1550.